Title: **Imaging decision-related neural cascades in the human brain**

Authors: Jordan Muraskin[1], Truman R. Brown[2], Jennifer M. Walz[3], Bryan Conroy[4], Robin I. Goldman[5], Paul Sajda[1]

[1] Department of Biomedical Engineering, Columbia University, New York, NY, USA 10027

[2] Center for Biomedical Imaging, Medical University of South Carolina, Charleston, SC, USA, 29425

[3] Florey Institute of Neuroscience and Mental Health, Melbourne, Australia

[4] Philips Research, New York, NY,

[5] Center for Healthy Minds, University of Wisconsin-Madison, Madison, WI, USA, 53705

Corresponding Author: Paul Sajda, psajda@columbia.edu

## *Abstract*

Perceptual decisions depend on coordinated patterns of neural activity cascading across the brain, running in time from stimulus to response and in space from primary sensory regions to the frontal lobe. Measuring this cascade and how it flows through the brain is key to developing an understanding of how our brains function. However observing, let alone understanding, this cascade, particularly in humans, is challenging. Here, we report a significant methodological advance allowing this observation in humans at unprecedented spatiotemporal resolution. We use a novel encoding model to link simultaneously measured electroencephalography (EEG) and functional magnetic resonance imaging (fMRI) signals to infer the high-resolution spatiotemporal brain dynamics taking place during rapid visual perceptual decision-making. After demonstrating the methodology replicates past results, we show that it uncovers a previously unobserved sequential reactivation of a substantial fraction of the pre-response network whose magnitude correlates with decision confidence. Our results illustrate that a temporally coordinated and spatially distributed neural cascade underlies perceptual decision-making, with our methodology illuminating complex brain dynamics that would otherwise be unobservable using conventional fMRI or EEG separately. We expect this methodology to be useful in observing brain dynamics in a wide range of other mental processes.

## *Introduction*

The detailed spatiotemporal brain dynamics that underlie human decision-making are difficult to measure. Invasive techniques with sufficient temporal or spatial resolution, such as depth electrodes or cortical arrays used with epilepsy patients, are only feasible in rare cases and, in addition, do not capture activity from the entire brain. In comparison, non-invasive measures such as electroencephalography (EEG) and magnetoencephalography (MEG) suffer from poor spatial resolution, and blood oxygen level dependent functional MRI (BOLD fMRI) from poor temporal resolution and indirect coupling to neural activity (e.g. fMRI)[1]. In spite of this, EEG, MEG, and fMRI have been used individually to study perceptual decision-making in the human brain, although, by themselves they provide a limited view of the underlying brain dynamics [2].

Recently, methods enabling simultaneous acquisition of EEG and fMRI (EEG/fMRI) have led to varied analytic approaches aimed at integrating the electrophysiological and hemodynamic information contained in the joint measurements. Such approaches offer the potential to provide a comprehensive picture of global brain dynamics, and will likely offer new insights into how the brain makes rapid decisions [3,4]. Some of the techniques that have been proposed for combining multi-modal brain signals have separately analyzed the EEG and fMRI data and subsequently juxtaposed the results[5,6], while others attempt for a truly integrated approach in order to fully exploit the joint information contained in the data sets [7]. In general, simultaneous EEG/fMRI and the associated analysis techniques have been used to identify neuronal sources of EEG trial-to-trial variability, linking them to cognitive processes such as attention [8] and inhibition [9].

Many previous studies have used known EEG markers (P1, N2, N170, P300, α-rhythm) or data driven approaches such as Independent Component Analysis (ICA) to combine EEG with fMRI data [4,8-16]. One promising approach has been to use supervised machine-learning techniques (e.g. classifiers) to find relevant projections of the EEG data, where single-trial variability of the electrophysiological response along these projections can be correlated in the fMRI space. Goldman, et al. [17], Walz, et al. [18] and Fouragnan, et al. [19] have demonstrated this technique on visual and auditory paradigms. This methodology has been shown to localize cortical regions that modulate with the task while preserving the temporal progression of task-relevant neural activity.

Here we combine a classification methodology with an encoding model that relates the trial-to-trial variability in the EEG to what is observed in the simultaneously acquired fMRI. Encoding models have become an important machine learning tool for analysis of neuroimaging data, specifically fMRI [20]. In most cases encoding models have been used to learn brain activity that encodes or represents features of a stimulus, such as visual orientation energy in an image/video [21-23], acoustic spectral power in sound/speech [24], or visual imagery during sleep [25]. In the method presented here, we employ an encoding model to directly relate the simultaneously collected data from the two neuroimaging modalities—instead of features derived from the stimulus, they are derived from EEG component trial-to-trial variability. Specifically, we learn an encoding in the spatially precise fMRI data from the temporally precise trial-to-trial variability of EEG activity predictive of the level of stimulus evidence. This approach leverages the fact that the level of stimulus evidence, as measured via EEG, persists across the trial [26,27], and

that by discriminating this information in a time-localized way, one can temporally "tag" specific cortical areas by their trial-to-trial variability.

Using our framework for learning the BOLD signal encoding of task-relevant and temporally precise EEG component variability, we unravel the cascade of activity from the representation of sensory input to decision formation, decision action, and decision monitoring. A particularly novel finding is that after the activation of decision monitoring regions (i.e. ACC), we see a reactivation of pre-response networks, where the strength of this reactivation correlates with measures of decision confidence. This specific reactivation, as well as the entire spatio-temporal cascade, is completely unobservable using conventional fMRI-only or EEG-only methodologies.

## *Results*

In this study, we used a visual alternative forced choice (AFC) task where subjects were shown brief presentations of pictures corrupted by noise and instructed to rapidly discriminate between object categories. On any given trial, the level of noise, or stimulus evidence, was varied randomly. The task itself, as well as similar visual decision-making tasks [28], is believed to engage an extensive set of cortical areas in a coordinated fashion, including regions that are responsible for sensory encoding, evidence accumulation, decision formation, and response and decision monitoring. However, the dynamic interplay of these regions has never been observed in humans. Here we exploit previously reported findings regarding the sensitivity of the EEG and fMRI signals to the level of stimulus evidence during a perceptual decision-making task. Specifically, previous work has shown differential neural responses to high vs. low

stimulus evidence in trial averaged EEG event-related potentials (ERPs), where this difference persists across the trial[26,27]. Similarly, fMRI studies have shown that for perceptual decision making tasks a number of spatially-distributed cortical areas significantly correlate with the level of stimulus evidence[29,30]. We leverage the fact that the level of stimulus evidence is expressed temporally in the EEG and spatially in the fMRI to "tag" voxels with a time. Specifically, using a classification methodology (i.e. discriminative components) we identify temporally precise expressions of the level of stimulus evidence that then can be spatially localized through an encoding model of the fMRI BOLD data.

We collected simultaneous EEG/fMRI data from 21 subjects as they performed a 3-AFC task discriminating between faces, cars, and houses (Fig. 1A). Subjects were instructed to discriminate the object class after briefly viewing an image corrupted by varying levels of noise (Fig. 1B) and respond by pressing one of three buttons. Overall, subjects responded with accuracies of 94 ± 5% and 58 ± 12% and with response times of 634 ± 82ms and 770 ± 99ms for high and low stimulus evidence trials, respectively (Fig. 1 C, D). Subject accuracies and response times across stimulus types (faces, cars, houses) for low stimulus evidence trials were similar; however, for high stimulus-evidence trials subject accuracies were higher and response times were shorter for faces than for cars or houses (See Supplemental Information Fig. S1).

*GLM based analysis of BOLD fMRI shows superposition of cortical areas correlated with stimulus evidence*

A traditional general linear model (GLM) analysis of the fMRI (see Methods) revealed differences in BOLD activation between the two stimulus evidence conditions (Fig. 1F, SI Table 1). Brain regions showing greater BOLD activation to high vs. low stimulus evidence trials included areas associated with early visual perception and the default mode network[26], such as fusiform gyrus, parahippocampal gyrus, lateral occipital cortex, superior frontal gyrus, and posterior cingulate cortex. Regions with greater BOLD activation to low vs. high stimulus evidence trials included areas in the executive control and difficulty networks, such as dorsal lateral prefrontal cortex, anterior cingulate cortex, intraparietal sulcus, and insula. Overall, these GLM results for the BOLD data reproduced previous results in the literature where similar stimuli and paradigms were used [29](Fig. S2A).

*Extracting temporally localized EEG signatures of stimulus evidence variability*

The traditional fMRI results showed multiple brain regions correlated with the difficulty, or stimulus evidence, of the trial; however, this traditional approach does not enable one to infer the relative timing of these fMRI activations. To infer timing at a scale of tens of milliseconds, we used linear classification[31,32] of the EEG to extract trial-to-trial variability related to stimulus evidence at specified post-stimulus time points.

The basic idea is illustrated in Figure 2, where hypothetical neural activity is shown for two different regions that are constituents of the perceptual decision-making network. Averaging over trials would clearly reveal a difference in the mean neural activity between high and low stimulus evidence. However, the two regions contribute differentially to the network, with one region encoding the stimulus evidence (Region 1)

and the other integrating it over time (Region 2); both are sensitive to the level of stimulus evidence, though varyingly so at different times in the trial. By taking advantage of this sensitivity to the stimulus evidence, we can learn EEG discriminant components, i.e. spatial filters, that best classify trials at different time windows given the neural data. We used the trial-to-trial variability along these component directions as features to uniquely tag fMRI voxels with the specific time window of the component. This tagging is done by building an encoding model of the features, given the BOLD signal, details of which are described in the following section.

We constructed EEG components by learning linear classifiers at 25ms steps, starting from stimulus onset to 50ms past the average low stimulus evidence response time. We chose a time step of 25ms due to an empirical analysis showing a half width of 50ms in the temporal autocorrelation of the EEG data, though in principle this methodology allows for temporal resolution up to the EEG sampling rate. Each classifier was associated with a set of discriminant values, which can be represented as a vector $y_\tau$; each element of the vector is the distance of a given trial to the discrimination boundary for the classifier at time step $\tau$ (Fig. 2). This distance can be interpreted as a measure of the EEG classifier's estimate of the level of stimulus evidence for that trial[17,18,31-34].

Results of the EEG analysis show discriminating information for stimulus evidence spanning the trial (see Fig. 4A), beginning roughly 175ms post-stimulus to past the average response times. A dip occurs around 300ms, indicating stimulus evidence is less discriminative at this time and serves to demarcate early and late cognitive processes. The early process corresponded to the time of the D220 ERP component, which has been shown to modulate with the degree of task difficulty, whether via stimulus noise or task

demands[35]. The later and more prolonged component is likely related to more complex cognitive and motor preparatory processes that differ between high and low stimulus evidence trials. Importantly, although the early and late EEG components were both discriminative, we found their trial-to-trial variability to be uncorrelated (Figs. 4B and S3E), indicating that while the discriminating information (level of stimulus evidence) persists across the trial, it couples differently to processes across time.

*An encoding model links fMRI activations with temporally distinct EEG trial-to-trial variability*

After extracting the trial-to-trial variability from the EEG discriminant components, feature vectors $y_\tau$ are collected across time steps, $\tau$, along with a response time vector to construct a matrix *Y*. This matrix is the temporally precise representation of the trial-to-trial EEG variability that reflects high vs. low stimulus evidence. An encoding model is then fit, namely a model in which weights are estimated for each time-localized EEG window, to predict the trial-to-trial variability of the BOLD response for each fMRI voxel. Figure 3 shows a schematic of the encoding model framework we used and compares it to a traditional encoding model constructed by using features derived directly from the stimulus. Rather than constructing a map that directly relates each voxel to a type of stimulus feature, such as whether it encodes edges, motion or some semantic concept such as "animal" [21-23,36-38], our model is used to construct maps that label voxels by the time window of the variability they encode – i.e. it "tags" each voxel with a "time", or set of times, when it encodes the variability in the given EEG discriminant component(s).

It is important to note that this approach does not attempt to improve source localization typically done for EEG/MEG studies. Our approach instead provides the temporal resolution of EEG (ms) and the spatial resolution of fMRI (mm) without the need to solve the ill-posed inverse solution and make the many associated assumptions required for reliable source-localization results[39].

An example of the quality of the encoding model is shown in Fig. 4C (see also Fig. S2B) where significant voxels from the encoding model are shown in yellow. Fig. 4D shows the trial-to-trial variability of BOLD signal at a specific voxel, comparing it to the variability predicted by the encoding model. Additional validity of the encoding model and single subject results are presented in the Supplemental Information (Fig. S4A/B). The encoding model was also evaluated as a decoding model (see Methods) with the BOLD activity used to predict the trial-to-trial variability in the EEG for unseen data—data on which the encoding model was not trained. Fig. 4E shows these results, expressed as the correlation between the measured and predicted EEG trial-to-trial variability across the 800ms epoch. The shape of the curve is highly consistent with that observed for the EEG data itself (comparing Fig. 4A and Fig. 4E) (additional analysis of the fidelity of the model is provided in the SI, Fig. S3).

Given the encoding model, we unwrap the BOLD activity across time by identifying weights that are consistent across subjects in space and time (see Methods). Fig. 5 shows these results for a group level analysis. We observe a progression of activity (see Movie S1), at 25ms resolution, which proceeds simultaneously down the dorsal and ventral streams of visual processing for the first 250ms. After that the cascade becomes more complex with activation in the IPS at 425ms and 750ms (see Fig. 6A), reactivation

of the SPL at 675ms and activation of ACC at 600ms along with other regions found in the traditional fMRI results. (see Fig. S5, Tables S2 and an additional analysis using dynamic causal modeling [40]). The reactivation pattern is particularly significant since it would not be observable via a traditional fMRI general linear model (GLM) analysis, which integrates over time and thus superimposes these activities. For example, the changing sign of the middle temporal gyrus (MT) encoding weights in Fig. 6A manifested as no activity in the MT for the traditional fMRI GLM analysis—the change in sign canceled the effective correlation in the GLM (see Fig. 1F and Fig. S1). The areas of activation we find are consistent with previous reports in the literature for human subjects[29,30]; however, here we are able to link activations across time in a way that was previously only possible with invasive techniques.

*Cortical reactivation correlates with decision confidence*

Further analysis of the spatiotemporal dynamics (see Fig. 6B), shows that the reactivation pattern in the network occurs after decision-monitoring areas become engaged (i.e. after ACC). Spontaneous reactivation, or "replay", of neural activity in the human brain has been observed and believed to be important for memory consolidation[41] and more recently has been hypothesized to play a role in perceptual decision-making by enabling the formation of decision confidence[42]. To test the hypothesis that the reactivation activity we see is in fact related to decision confidence, we used a hierarchical drift diffusion model (DDM)[43,44] to fit the behavioral data for high and low stimulus evidence conditions (see Methods). Specifically, our model enables us to define a proxy for decision confidence based on the DDM fits to the behavior[45,46]. Correlating

245 the reactivation level to this confidence proxy shows a strong and significant monotonic
246 relationship between confidence and the level of reactivation (high stimulus evidence-
247 slope=0.037±0.008, t=4.657, $p=3.2x10^{-6}$; low stimulus evidence-slope=0.062±0.008,
248 t=7.754, $p=8.88x10^{-15}$), with low stimulus evidence trials reactivated more strongly than
249 high stimulus evidence trials (difference in slopes=-0.025±0.011, t=2.189, p=0.029)(see
250 Fig. 7 and Fig. S7). Additionally, reactivation amplitude correlates with behavioral
251 accuracy (Fig. S8) (high stimulus evidence, slope=0.0115±0.0047, t=2.41, p=0.016; low
252 stimulus evidence, slope=0.0104±0.0047, t=2.19, p=0.028). Recursive feature elimination
253 showed that the IPS/SPL and dorsal lateral prefrontal cortex (DLPFC) clusters
254 contributed the most to reactivation/confidence proxy correlation (Fig. 7C).
255
256

257 ***Discussion***

258 We have shown that linking simultaneously acquired EEG and fMRI using a novel
259 encoding model enables imaging of high-resolution spatiotemporal dynamics that
260 underlie rapid perceptual decision-making — decisions made in less than a second. This
261 method, which resolves whole-brain activity with EEG-like temporal resolution, was
262 shown to uncover reactivation processes that would otherwise be masked by the temporal
263 averaging and slow dynamics of traditional fMRI. More broadly, our results
264 demonstrated a general non-invasive data-driven methodology for measuring high
265 spatiotemporal latent neural processes underlying human behavior.

266 This approach temporally "tags" the BOLD fMRI data by encoding the trial-to-
267 trial variability of the temporally precise task relevant components in simultaneously

acquired EEG. In effect, the EEG discrimination indexes the activity of interest at high temporal resolution, defining a feature space, and the trial-to-trial variability of these discriminant components becomes the specific feature values used in the encoding model. For the case presented here, this variability was used to tease apart the cascade of activity modulated by stimulus evidence across the trial, and this allowed us to observe, as never seen before, the spatiotemporal brain dynamics underlying a perceptual decision.

Previous studies have sought to generalize the timing diagram of a perceptual decision through multi-unit recordings in non-human primates[47,48] or more broadly in humans[29,30] using fMRI. Our results confirmed the general temporal ordering of activations found previously (early visual processing, decision formation, decision monitoring). However, there was a possibility the temporal order we observed using our technique was an artifact of our methodology. To assess this possibility, we performed additional analyses using dynamic causal modeling (DCM) to further validate the temporal activation sequence (see Fig. S6) and show, using a different set of assumptions and method, that the temporal sequence we observe is highly likely under a set of alternative sequences. We found that the most likely model is the one consistent with the time course inferred from our encoding model. The DCM results provide additional evidence that the temporal profile uncovered by the encoding model is a likely temporal decomposition of the superimposed fMRI activations.

The approach we present requires that EEG and BOLD data be collected simultaneously and not in separate sessions in order to exploit the correlations in trial-to-trial variability to "tag" the BOLD data. To show the importance of collecting the data simultaneously, we ran a control analysis that randomly permuted the trials within their

stimulus evidence class, thus effectively simulating an EEG and BOLD dataset collected separately. By destroying the link between the EEG and BOLD trials, the encoding model failed to find any consistent activation (Fig. S11/12), indicating the necessity of simultaneous acquisition.

Alternative techniques for fusing simultaneous EEG-fMRI typically do not exploit EEG across the trial and instead only analyze specific ERP components or time windows of interest [4,8,10,12-19,49,50]. Results from these techniques identify regions that modulate with the specific components, but yield limited information about the timing of other task-relevant regions seen in traditional fMRI contrasts. The methodology developed here extends the work of Goldman, et al. [17] and Walz, et al. [18] by combining their EEG data reduction techniques with techniques developed for encoding stimulus features onto BOLD data[20-23,36,38], ultimately providing a framework for labeling voxels in task-relevant fMRI contrasts with their timing information (Fig. S2C/E/F).

Clearly, other EEG components that are task-related can be isolated and could potentially be used to "tag" BOLD data. The sliding window linear classification used here acts to reduce the EEG data along a dimension that categorizes stimulus evidence; however, this could be replaced by any other data reduction technique, such as temporally windowed ICA or PCA. Variability along these component directions could then be used in the encoding model to link with the simultaneously collected BOLD data. The choice of data reduction technique (i.e. feature space) would be highly dependent on the nature of the inferences.

Our methodology enabled us to observe reactivation of the pre-response network, spatiotemporal dynamics that would be masked using traditional fMRI analysis.

Interestingly, the reactivation terminated in a network that included the MFG, SPL, and IPS, similar areas previously reported to be reactivated in metacognitive judgments of confidence in perceptual decisions[42,51,52]. In addition, these areas contributed the most to the correlation to confidence proxy (Fig. 7C). Gherman and Philiastides [53] observed this network using a multivariate single-trial EEG approach, coupled with a distributed source reconstruction technique. Fleming, et al. [42] and Heereman, et al. [54] used BOLD fMRI to show that areas in this network negatively correlate with subjective certainty ratings. Unique to our findings, we saw this reactivation on a single-trial basis after engagement of the ACC, which has been shown to be involved in decision monitoring[53,55], and also observed the dynamic sequence leading up to this network reactivation. Our results showed that reactivation/replay occurred on a trial-to-trial basis after a decision, was stronger for difficult decisions, and correlated with decision confidence.

A potential confound in our analysis is that the timing of the reactivation overlaps with some of the response times. To check if the reactivation was pre or post response, we implemented a response-locked encoding model analysis (Fig. S9). The response-locked results showed significant activation pre-response that overlaps with the reactivation network from the stimulus locked analysis. In addition, trial-to-trial reactivation taken from pre-response clusters correlates with confidence proxy similarly to the stimulus locked results (Fig. S10). This provides further evidence that the reactivation is occurring pre-response.

The encoding model we developed was able to decompose traditional fMRI activation maps into their temporal order with significant voxel overlap between the encoding model results and traditional results. The encoding model was also able to show

337 regions that were activated at multiple time points throughout the decision, indicating
338 temporal dynamics that were hidden previously. The regions of activation we found are
339 consistent with earlier findings; however, the work here provided the precise temporal
340 decomposition of these previously reported, temporally superimposed regions of
341 activation. In general, we have shown that simultaneously acquired EEG/fMRI data
342 enables a novel non-invasive approach to visualize high resolution spatial and temporal
343 processing in the human brain with the potential for providing a more comprehensive
344 understanding of the neural basis of complex behaviors.
345

346 ## *Methods*

347 *Subjects*

348 21 subjects (12 male, 9 female; age range 20-35 years) participated in the study. The
349 Columbia University Institutional Review Board (IRB) approved all experiments and
350 informed consent was obtained before the start of each experiment. All subjects had
351 normal or corrected-to-normal vision.

352 *Stimuli*

353 We used a set of 30 face (from the Max Planck Institute face database), 30 car, and 30
354 house (obtained from the web) gray scale images (image size 512x512 pixels, 8
355 bits/pixel). They were all equated for spatial frequency, luminance, and contrast. The
356 stimulus evidence (high or low) of the task was modulated by systematically modifying
357 the salience of the image via randomization of image phase (35% (low) and 50% (high)
358 coherence)[56].

359 *Experimental task*

The stimuli were used in an event-related three-alternative forced choice (3-AFC) visual discrimination task. On each trial, an image -- either a face, car, or house -- was presented and subjects were instructed to respond with the category of the image by pressing one of three buttons on an MR compatible button controller. Stimuli were presented to subjects using E-Prime software (Psychology Software Tools) and a VisuaStim Digital System (Resonance Technology) with 600x800 goggle display. Over four runs, a total of 720 trials were acquired (240 of each category with 120 high coherence trials) with a random inter-trial interval (ITI) sampled uniformly between 2-2.5s. Each run lasted for 560 seconds.

*fMRI acquisition*

Blood-oxygenation-level-dependent (BOLD) T2*-weighted functional images were acquired on a 3T Philips Achieva scanner using a gradient-echo echo-planar imaging (EPI) pulse sequence with the following parameters: Repetition time (TR) 2000ms, echo time (TE) 25ms, flip angle 90°, slice thickness 3mm, interslice gap 1mm, in-plane resolution 3x3mm, 27 slices per volume, 280 volumes. For all of the participants, we also acquired a standard T1-weighted structural MRI scan (SPGR, resolution 1x1x1mm).

*EEG acquisition*

We simultaneously and continuously recorded EEG using a custom-built MR-compatible EEG system[57,58], with differential amplifiers and bipolar EEG montage. The caps were configured with 36 Ag/AgCl electrodes including left and right mastoids, arranged as 43 bipolar pairs. Bipolar pair leads were twisted to minimize inductive pickup from the magnetic gradient pulses and subject head motion in the main magnetic field. This oversampling of electrodes ensured data from a complete set of electrodes even in

383 instances when discarding noisy channels was necessary. To enable removal of gradient
384 artifacts in our offline preprocessing, we synchronized the EEG with the scanner clock by
385 sending a transistor– transistor logic pulse at the start of each image volume. All
386 electrode impedances were kept below 20 kΩ, which included 10 kΩ resistors built into
387 each electrode for subject safety.
388 *Functional image pre-processing.*
389 Image preprocessing was performed with FSL (www.fmrib.ox.ac.uk/fsl/). Functional
390 images were spatially realigned to the middle image in the times series (motion-
391 correction), corrected for slice time acquisition, spatially smoothed with a 6mm FWHM
392 Gaussian kernel, and high pass filtered (100s). The structural images were segmented
393 (into grey matter, white matter and cerebro-spinal fluid), bias corrected and spatially
394 normalized to the MNI template using 'FAST' [59]. Functional images were registered into
395 MNI space using boundary based registration (BBR)[60].
396
397 *EEG data preprocessing.*
398 We performed standard EEG preprocessing offline using MATLAB (MathWorks) with
399 the following digital Butterworth filters: 0.5 Hz high pass to remove direct current drift,
400 60 and 120 Hz notches to remove electrical line noise and its first harmonic, and 100 Hz
401 low pass to remove high-frequency artifacts not associated with neurophysiological
402 processes. These filters were applied together in the form of a zero-phase finite impulse
403 response filter to avoid distortions caused by phase delays. We extracted stimulus-locked
404 1500 ms epochs (-500:1000) and subtracted the mean baseline – -200 ms to stimulus
405 onset – from the rest of the epoch. Through visual inspection, we discarded trials

406 containing motion and/or blink artifacts, evidenced by sudden high-amplitude
407 deflections.

408 *Sliding window logistic regression.*

409 We used linear discrimination to associate each trial with the level of stimulus evidence
410 represented in the EEG. We considered high stimulus and low stimulus evidence trials
411 irrespective of behavioral accuracy. Regularized logistic regression was used as a
412 classifier to find an optimal projection for discriminating between high and low stimulus
413 evidence trials over a specific temporal window. A sweep of the regularization
414 parameters was implemented using FaSTGLZ[61]. This approach has been previously
415 applied to identify neural components underlying rapid perceptual decision-making
416 [17,18,31,33,34,45,50,62].

417 Specifically, we defined 50ms duration training windows centered at time, $\tau$,
418 ranging from stimulus onset to 800ms following the stimulus in 25ms steps. We used
419 logistic regression to estimate a spatial weighting, on N EEG channels, vector ($w_\tau$ which
420 is N x 1) that maximally discriminated between EEG sensor array signals E for each class
421 (e.g., high vs. low stimulus evidence trials):

422 $$y_\tau = w_\tau^T E_\tau \quad (1)$$

423 In eqn. 1, $E_\tau$ is an N x p vector (N sensors per time window $\tau$ by p trials). For our
424 experiments, the center of the window ($\tau$) was varied across the trial in 25ms time-steps.
425 We quantified the performance of the linear discriminator by the area under the receiver
426 operator characteristic (ROC) curve, referred to here as AUC, using a leave-one-out
427 procedure. We used the ROC AUC metric to characterize the discrimination performance
428 as a function of sliding our training window (i.e., varying $\tau$). For each subject, this

429 produced a matrix Y where the rows corresponded to trials and the columns to training
430 windows, i.e. Y is the combination of the calculated $y_\tau$ for each time window.
431 *Traditional fMRI analysis.*
432 We first ran a traditional general linear model (GLM) fMRI analysis in FSL, using
433 event-related (high and low stimulus evidence) and response time (RT) variability
434 regressors. The event-related regressors comprised boxcar functions with unit amplitude
435 and onset and offset matching that of the stimuli. RT variability was modeled using the z-
436 scored RT as the amplitude of the boxcars with onset and offset matching that of the
437 stimulus, and these were orthogonalized to the event-related regressors.
438 Orthogonalization was implemented using the Gram-Schmidt procedure[63] to decorrelate
439 the RT regressor from all other event-related regressors. All regressors were convolved
440 with the canonical hemodynamic response function (HRF), and temporal derivatives
441 were included as confounds of no interest. An event-related high versus low stimulus
442 evidence contrast was also constructed. A fixed-effects model was used to model
443 activations across runs, and a mixed-effects approach was used to compute the contrasts
444 across subjects. Activated regions that passed a family-wise error (FWE) [64] corrected
445 cluster threshold of $p < 0.01$ at a z-score threshold of 2.57 were considered significant.
446 *fMRI deconvolution.*
447 Associating fMRI data to each trial is challenging for two main reasons: (a) the temporal
448 dynamics of the hemodynamic response function (HRF) evolve over a longer time-scale
449 than the mean ITI of the event-related design, resulting in overlapping responses between
450 adjacent trials; and (b) the ITI was random for each trial so that the fMRI data was not
451 acquired at a common lag relative to stimulus onset. To overcome these issues, we

452 employed the `least squares - separate' (LS-S) deconvolution[65] method to estimate the
453 voxel activations for each trial. For every trial, the time series of each voxel was
454 regressed against a “signal" regressor and a “noise" regressor. The “signal" regressor was
455 the modeled HRF response due to that trial (a delta function centered at stimulus onset
456 convolved with a canonical HRF), while the “noise" regressor was the modeled HRF
457 response due to all other trials (superimposed linearly). The resulting regression
458 coefficients of the “signal" regressor represented the estimated voxel activations due to
459 that trial. These voxel activations were then organized into a single brain volume per trial.
460 We extracted 58697 voxels from a common gray matter group mask at 3 $mm^3$ spatial
461 resolution that excluded white matter and CSF and assembled the resulting voxel
462 activations into rows of the data matrix F.

463 *Single subject encoding model.*

464 All encoding model analyses were performed in MATLAB. To relate the EEG data with
465 the fMRI, we devised a subject-wise spatio-temporal decomposition using singular value
466 decomposition (SVD). Let F be an m x p matrix denoting m-voxels and p-trials that is the
467 deconvolved high and low stimulus evidence fMRI data for each trial. Let Y be the r x p
468 matrix denoting r-windows (33 $EEG_\tau$ windows and response time (RT)) and p-trials. For
469 each trial, the first row of Y is the response times while subsequent rows are the y values
470 at each window time. Let W be an m x r matrix that is the weights on Y that solve for F.

471 $$F = WY \quad (2)$$

472 Normally, if we solve for W using the least squares approach, we get:

473 $$W=(FY^T)(YY^T)^{-1} \quad (3)$$

However, each time point might be highly correlated with its neighbors, which reduces the stability of the least-squares regression. We can use SVD to reduce the feature space and improve our estimation of W (the weights on each window). Then for a leave-one-out cross validation, we hold out a single trial from the EEG Y matrix and the corresponding volume from the fMRI data F and train on the remaining trials. We repeated this for all trials.

$$Y^{Train}=U\Sigma V^{T} \quad (4)$$

Where U is an r x r orthonormal matrix, Σ is a r x p diagonal matrix and V is a p x p orthonormal matrix. After SVD on $Y^{Train}$, we reduced the feature dimensions on $Y^{Train}$ to retain 75% of the variance by only keeping v components. To do this, we selected the first v rows of Σ and zeroed the other rows. We now have $\tilde{\Sigma}$ as our reduced spaced matrix. If we now recalculate our least squares solution where we have replaced Y by its reduced form $U\tilde{\Sigma}V^{T}$ in equation 3:

$$\hat{W} = (F^{Train}V\tilde{\Sigma}^{T})(\Sigma\Sigma^{T})^{-1}U^{T} \quad (5)$$

So for each leave one out fold, we first calculated the SVD of the training set. We then calculated the number of components to keep and then solve for $\hat{W}$, the weight estimate per fold. To test, we then applied the weights to the left-out test data $Y^{Test}$ to estimate the encoded fMRI data $\hat{F}$ for the encoding part:

$$\hat{F} = \hat{W}Y^{Test} \quad (6)$$

While for the decoding model using the left out test data $F^{Test}$:

$$\hat{Y} = \hat{W}^{T}F^{Test}(\hat{W}^{T}\hat{W})^{+} \quad (7)$$

Here, $\hat{W}^{T}\hat{W}$ is not invertible, and so we used the pseudo-inverse.

At this point, we have $\hat{F}$, a m x p matrix with m voxels by p trials. For each voxel j, we calculated the correlation of $\hat{F}_j$ with $F_j$, resulting in the matrices $R^{fMRI}$ (Pearson Correlation Map) and $P^{fMRI}$ (p-value map of the Pearson Correlation) that are m x 1. The $P^{fMRI}$ was then converted to a z-score map. We constructed the m x r weight matrix W by taking the average of all the trained $\hat{W}$ matrices. To test which time windows were significant, we also calculated, $R_\tau^{EEG}$, the correlation between $\hat{Y}_\tau$ and $Y_\tau$.

*Group level spatio-temporal analysis.*

For group level statistics, we first analyzed the $R_\tau^{EEG}$ vectors across all subjects. The $R_\tau^{EEG}$ vectors were converted into their p-values, and for each time window ($\tau$), used to compute combined Stouffer p-values [66]. These group level results were then false discovery rate corrected (FDR) for multiple comparisons[67]. To identify group level voxels where our model predictions were significant, each subject's p-value maps for the leave-one-out correlation were converted into their respective z-values, and voxel-wise significance was calculated using threshold-free cluster enhancement (TFCE) using a non-parametric randomization procedure implemented in FSL[68]. Voxels were considered significant if they passed a conservative false discovery rate threshold of $p<0.01$.

These significant voxels were then used as a mask to temporally localize activations by computing the voxels that were consistent in their direction ( positive (high stimulus evidence) or negative (low stimulus evidence) ) and timing ($\tau$ window). To this end, we implemented a spatio-temporal TFCE (stTFCE) in both space (neighboring voxels) and time (neighboring time windows - response time window not included) and computed significance through a randomization procedure. 33000 permutations (1000 permutations per window) were run by randomly altering the sign of each subject and the

519 temporal ordering of the windows, as we were testing whether the weights were
520 consistent in sign, voxel space, and temporal window. P-values were calculated by
521 comparing the true stTFCE value with the distribution of permuted values. Again, voxels
522 were considered significant if they passed FDR correction at $p<0.05$ (high stimulus
523 evidence: FDR-Corrected $p<0.0019$, low stimulus evidence: FDR-Corrected $p<0.00036$).
524 Note, that now our number of multiple comparisons was the number of voxels in the
525 FDR-mask (20256) times the number of time windows (33). We analyzed the response
526 time separately with a standard TFCE randomization procedure implemented in FSL
527 (Fig. S2D).
528 *Dynamic causal modeling.*
529 To validate the encoding model timing, we implemented single-state linear
530 dynamic causal modeling (DCM) using DCM10 in SPM8 [69], and applied this to the
531 BOLD data to test the hypothesis that the temporal sequence of BOLD activations we
532 found in our EEG-fMRI encoding method was most likely, relative to other possible
533 sequences of these same activations, given only the BOLD data. We used the results of
534 the encoding model to select seven regions of interest that spanned the entire trial. For the
535 first region (labeled 175 in our figures), we computed the union of activations during the
536 175ms and 200ms windows. Activations of the 225ms (225) and 250ms combined with
537 275ms (250) windows become the second and third regions. We computed the union of
538 activations during the 325ms and 350ms windows to create the fourth (325). For the fifth
539 region (400), we computed the union of the activations during the 400ms-450ms
540 windows. For the sixth region (650), we computed the union of the activations during the
541 650ms and 675ms windows. Finally, the union of the activations during the 725-800ms

542 windows was computed to create the seventh region (725). We removed any overlapping
543 voxels between any of the regions and then extracted time series from individual
544 subjects' preprocessed functional data in MNI space by estimation of the first principal
545 component within each region.

546 We constructed 11 models (Figure S6) to investigate the directed connectivity of
547 these regions and validate the temporal ordering found by the encoding model. Each
548 model was feed-forward with first node in each model as the input region. The first
549 model was the temporal ordering of the regions inferred from our EEG-fMRI encoding
550 model analysis. For five of the models, we randomized the temporal ordering of the early
551 regions (175, 225, 250) and the late regions (325, 400, 650, 725) separately. For the other
552 five models, we fully randomized the temporal ordering of all the regions.

553 We used fixed-effects Bayesian model selection (BMS) to compare these 11
554 models both on a single-subject level and at the group level. BMS balances model fit and
555 complexity, thereby selecting the most generalizable model. It estimates the relative
556 model evidence and provides a distribution of posterior probabilities for all of the models
557 considered. We also compared families of similar models[70]; the model space was divided
558 into two families (early/late or fully randomized).

559

560 *Drift Diffusion Model (DDM) and Confidence Proxy.*

561 The DDM models decision-making in two-choice tasks. Here, we treated the decision
562 (correct vs. incorrect) as our two choices. A drift-process accumulates evidence over time
563 until it crosses one of two boundaries (upper or lower) and initiates the corresponding
564 response[68]. The speed with which the accumulation process approaches one of the two

565 boundaries (a) is called drift-rate (v) and represents the relative evidence for or against a
566 particular response. Recently, Philiastides, et al. [45] showed that for conditions in which
567 the boundary (a) does not change, a proxy for decision confidence for each trial (i) can be
568 computed by $1/\sqrt{RT_i - T_{non}}$.

569 We used Hierarchical Bayesian estimation of the Drift-Diffusion Model in Python
570 (HDDM) to calculate the drift rate (v), decision boundary (a) and non-decision time $T_{non}$
571 for each subject [43]. Specifically, we modeled high and low stimulus evidence response
572 time data separately. This was to ensure our confidence proxies were consistent within
573 trial types. We included the response time and whether the subject got the trial correct.
574 HDDM obtains a sequence of samples (i.e., a Markov chain Monte Carlo; MCMC) from
575 the posterior of each parameter in the DDM. In our model, we generated 5000 samples
576 from the posteriors, the first 1000 (burn-in) samples were discarded, and the remaining
577 samples were thinned by 5%.

578 After modeling the DDM process, each trial's (i) confidence proxy (CP) for each
579 subject (j) was computed by $CP_{i,j} = 1/\sqrt{RT_i - T_{non,j}}$ and then z-scored across trials where
580 $T_{non,j}$ was varied for high or low stimulus evidence trials, separately. Therefore, CP was a
581 measure of relative trial confidence within difficulty levels.
582
583 *Confidence Proxy and Decision Replay.*

584 Trial to trial reactivation amplitude was defined as $Y^R_{j,i} = W^T_{j,PostACC} F_{j,i}$ for each
585 subject (j) and trial (i), where $W_{postACC}$ is the weight matrix from the encoding model
586 thresholded by voxels that were significant in the group results from the 600-800ms

windows. The mean of the $Y^R_{j,i}$ across time becomes a measure of "decision replay" strength for that trial (more negative y's indicate more replay activation, more positive y's indicate less replay activation). $Y^R_{j,i}$ was quintiled for high and low stimulus evidence and the average confidence proxy was calculated within each quintile (Fig. 7). A linear mixed effects model[71] was used to test if the slope of confidences across quintile grouping, $Y^R_{j,i}$, were significantly different from 0 while including stimulus evidence as a condition. Separate similar analyses with non-replay windows (175-250ms) and testing for behavioral accuracy were also performed (Fig. S7-8). To test the contribution of each cluster to the correlation with confidence, we implemented recursive feature elimination, where our features were clusters of significant voxels (> 48 voxels) during the 600-800ms time window. This procedure removed clusters from the 'replay' network before calculating trial-to-trial reactivation. We then calculated the percent change in slope (reactivation x confidence proxy) when the cluster was removed compared to the total network. This procedure ranks cluster importance by sorting which clusters, when removed, had the strongest negative effect on slope height.

## *Author Contributions*

Conceptualization, J.M. and P.S.; Methodology, J.M., T.R.B., J.W. B.C., R.I.G. and P.S.; Investigation, J.M.; Software, J.M., B.C.;Writing – Original Draft, J.M. and P.S.; Writing – Review & Editing, J.M., T.R.B., R.I.G., J.W., and P.S. ; Funding Acquisition, P.S. ; Resources, J.M., T.R.B., J.W. B.C., R.I.G. and P.S.; Supervision, T.R.B and P.S.

## *Acknowledgements*

We would like to thank Jianing Shi for assistance in collecting the EEG/fMRI data. This work was funded by National Institutes of Health Grant R01-MH085092, DARPA under Contract NBCHC090029 and the Army Research Laboratory and under Cooperative Agreement Number W911NF-10-2-0022.

## *References*

1 Logothetis, N. K. What we can do and what we cannot do with fMRI. *Nature* **453**, 869-878, doi:10.1038/nature06976 (2008).

2 Alexander, D. M., Trengove, C. & van Leeuwen, C. Donders is dead: cortical traveling waves and the limits of mental chronometry in cognitive neuroscience. *Cognitive Processing*, doi:10.1007/s10339-015-0662-4 (2015).

3 Jorge, J. o., van der Zwaag, W. & Figueiredo, P. c. EEG-fMRI integration for the study of human brain function. *NeuroImage* **102**, 24--34, doi:10.1016/j.neuroimage.2013.05.114 (2014).

4 Huster, R. J., Debener, S., Eichele, T. & Herrmann, C. S. Methods for simultaneous EEG-fMRI: an introductory review. *The Journal of neuroscience : the official journal of the Society for Neuroscience* **32**, 6053-6060, doi:10.1523/jneurosci.0447-12.2012 (2012).

5 Plichta, M. M. *et al.* Simultaneous EEG and fMRI Reveals a Causally Connected Subcortical-Cortical Network during Reward Anticipation. *Journal of Neuroscience* **33**, 14526-14533, doi:10.1523/jneurosci.0631-13.2013 (2013).

6 Yuan, H. *et al.* Negative covariation between task-related responses in alpha/beta-band activity and BOLD in human sensorimotor cortex: an EEG and fMRI study of motor imagery and movements. *NeuroImage* **49**, 2596-2606, doi:10.1016/j.neuroimage.2009.10.028 (2010).

7 Dahne, S. *et al.* Multivariate Machine Learning Methods for Fusing Multimodal Functional Neuroimaging Data. *Proceedings of the IEEE* **103**, 1507-1530, doi:10.1109/JPROC.2015.2425807 (2015).

8 Warbrick, T., Arrubla, J., Boers, F., Neuner, I. & Shah, N. J. J. J. Attention to Detail: Why Considering Task Demands Is Essential for Single-Trial Analysis of BOLD Correlates of the Visual P1 and N1. *Journal of cognitive neuroscience* **26**, 1--14, doi:10.1162/jocn (2013).

9 Baumeister, S. *et al.* Sequential inhibitory control processes assessed through simultaneous EEG-fMRI. *NeuroImage*, doi:10.1016/j.neuroimage.2014.01.023 (2014).

10 Novitskiy, N., Ramautar, J. R. & Vanderperren, K. a. The BOLD correlates of the visual P1 and N1 in single-trial analysis of simultaneous EEG-fMRI recordings during a spatial detection task. *NeuroImage* **54**, 824--835, doi:10.1016/j.neuroimage.2010.09.041 (2010).

11 Nguyen, V. T. & Cunnington, R. The superior temporal sulcus and the N170 during face processing: Single trial analysis of concurrent EEG-fMRI. *NeuroImage*, doi:10.1016/j.neuroimage.2013.10.047 (2013).

12 De Martino, F. *et al.* Multimodal imaging: an evaluation of univariate and multivariate methods for simultaneous EEG/fMRI. *Magnetic resonance imaging* **28**, 1104-1112, doi:10.1016/j.mri.2009.12.026 (2010).

13 Mayhew, S. D., Ostwald, D., Porcaro, C. & Bagshaw, A. P. Spontaneous EEG alpha oscillation interacts with positive and negative BOLD responses in the visual-auditory cortices and default-mode network. *NeuroImage* **76**, 362-372, doi:10.1016/j.neuroimage.2013.02.070 (2013).

14 Jann, K. *et al.* BOLD correlates of EEG alpha phase-locking and the fMRI default mode network. *NeuroImage* **45**, 903-916, doi:10.1016/j.neuroimage.2009.01.001 (2009).

15 Jaspers-Fayer, F., Ertl, M., Leicht, G., Leupelt, A. & Mulert, C. Single-trial EEG-fMRI coupling of the emotional auditory early posterior negativity. *NeuroImage* **62**, 1807-1814, doi:10.1016/j.neuroimage.2012.05.018 (2012).

16 Omata, K., Hanakawa, T., Morimoto, M. & Honda, M. Spontaneous Slow Fluctuation of EEG Alpha Rhythm Reflects Activity in Deep-Brain Structures: A Simultaneous EEG-fMRI Study. *PloS one* **8**, e66869-e66869, doi:10.1371/journal.pone.0066869 (2013).

17 Goldman, R. I. *et al.* Single-trial discrimination for integrating simultaneous EEG and fMRI: identifying cortical areas contributing to trial-to-trial variability in the auditory oddball task. *NeuroImage* **47**, 136-147, doi:10.1016/j.neuroimage.2009.03.062 (2009).

18 Walz, J. M. *et al.* Simultaneous EEG-fMRI Reveals Temporal Evolution of Coupling between Supramodal Cortical Attention Networks and the Brainstem. *The Journal of neuroscience : the official journal of the Society for Neuroscience* **33**, 19212-19222, doi:10.1523/jneurosci.2649-13.2013 (2013).

19 Fouragnan, E., Retzler, C., Mullinger, K. & Philiastides, M. G. Two spatiotemporally distinct value systems shape reward-based learning in the human brain. *Nature communications* **6**, 8107, doi:10.1038/ncomms9107 (2015).

20 Naselaris, T., Kay, K. N., Nishimoto, S. & Gallant, J. L. Encoding and decoding in fMRI. *NeuroImage* **56**, 400-410, doi:10.1016/j.neuroimage.2010.07.073 (2011).

21 Hansen, K. A., Kay, K. N. & Gallant, J. L. Topographic organization in and near human visual area V4. *Journal of Neuroscience* **27**, 11896--11911, doi:10.1523/JNEUROSCI.2991-07.2007 (2007).

22 Kay, K. N., Naselaris, T., Prenger, R. J. & Gallant, J. L. Identifying natural images from human brain activity. *Nature* **452**, 352--355, doi:10.1038/nature06713 (2008).

23 Nishimoto, S. *et al.* Reconstructing visual experiences from brain activity evoked by natural movies. *Current Biology* **21**, 1641--1646, doi:10.1016/j.cub.2011.08.031 (2011).

24 Silbert, L. J., Honey, C. J., Simony, E., Poeppel, D. & Hasson, U. Coupled neural systems underlie the production and comprehension of naturalistic narrative speech. *Proceedings of the National Academy of Sciences* **111**, E4687--E4696, doi:10.1073/pnas.1323812111 (2014).

25 Horikawa, T., Tamaki, M., Miyawaki, Y. & Kamitani, Y. Neural decoding of visual imagery during sleep. *Science (New York, N.Y.)* **340**, 639-642, doi:10.1126/science.1234330 (2013).

26 Philiastides, M. G., Ratcliff, R. & Sajda, P. Neural representation of task difficulty and decision making during perceptual categorization: a timing diagram. *The Journal of neuroscience : the official journal of the Society for Neuroscience* **26**, 8965-8975, doi:10.1523/JNEUROSCI.1655-06.2006 (2006).

27 Banko, E. M., Gal, V., Kortvelyes, J., Kovacs, G. & Vidnyanszky, Z. Dissociating the effect of noise on sensory processing and overall decision difficulty. *The Journal of neuroscience : the official journal of the Society for Neuroscience* **31**, 2663-2674, doi:10.1523/JNEUROSCI.2725-10.2011 (2011).

28 Erickson, D. T. & Kayser, A. S. The neural representation of sensorimotor transformations in a human perceptual decision making network. *NeuroImage* **79C**, 340-350, doi:10.1016/j.neuroimage.2013.04.085 (2013).

29 Heekeren, H. R., Marrett, S., Bandettini, P. a. & Ungerleider, L. G. A general mechanism for perceptual decision-making in the human brain. *Nature* **431**, 859-862, doi:10.1038/nature02966 (2004).

30 Philiastides, M. G. & Sajda, P. EEG-informed fMRI reveals spatiotemporal characteristics of perceptual decision making. *The Journal of neuroscience : the official journal of the Society for Neuroscience* **27**, 13082-13091, doi:10.1523/JNEUROSCI.3540-07.2007 (2007).

31 Parra, L. C., Spence, C. D., Gerson, A. D. & Sajda, P. Recipes for the linear analysis of EEG. *NeuroImage* **28**, 326-341, doi:10.1016/j.neuroimage.2005.05.032 (2005).

32 Sajda, P., Philiastides, M. G. & Parra, L. C. Single-trial analysis of neuroimaging data: inferring neural networks underlying perceptual decision-making in the human brain. *IEEE Rev Biomed Eng* **2**, 97-109, doi:10.1109/RBME.2009.2034535 (2009).

33 Muraskin, J., Sherwin, J. & Sajda, P. Knowing when not to swing: EEG evidence that enhanced perception-action coupling underlies baseball batter expertise. *NeuroImage* **123**, 1-10, doi:10.1016/j.neuroimage.2015.08.028 (2015).

34 Sherwin, J., Muraskin, J. & Sajda, P. You Can't Think and Hit at the Same Time: Neural Correlates of Baseball Pitch Classification. *Frontiers in neuroscience* **6**, 177, doi:10.3389/fnins.2012.00177 (2012).

35 Philiastides, M. G. & Sajda, P. Temporal characterization of the neural correlates of perceptual decision making in the human brain. *Cereb Cortex* **16**, 509-518, doi:10.1093/cercor/bhi130 (2006).

36 Cukur, T., Nishimoto, S., Huth, A. G. & Gallant, J. L. Attention during natural vision warps semantic representation across the human brain. *Nature neuroscience* **16**, 763-770, doi:10.1038/nn.3381 (2013).

37 Naselaris, T., Kay, K. N., Nishimoto, S. & Gallant, J. L. Vol. 56 400-410 (2011).

38 Stansbury, D., Naselaris, T. & Gallant, J. Natural Scene Statistics Account for the Representation of Scene Categories in Human Visual Cortex. *Neuron* **79**, 1025--1034, doi:10.1016/j.neuron.2013.06.034 (2013).

39 Wendel, K. *et al.* EEG/MEG source imaging: methods, challenges, and open issues. *Computational intelligence and neuroscience*, 656092, doi:10.1155/2009/656092 (2009).

40 Friston, K. J., Harrison, L. & Penny, W. Dynamic causal modelling. *NeuroImage* **19**, 1273--1302, doi:10.1016/S1053-8119(03)00202-7 (2003).

41 Deuker, L. *et al.* Memory consolidation by replay of stimulus-specific neural activity. *The Journal of neuroscience : the official journal of the Society for Neuroscience* **33**, 19373-19383, doi:10.1523/JNEUROSCI.0414-13.2013 (2013).

42 Fleming, S. M., Huijgen, J. & Dolan, R. J. Prefrontal contributions to metacognition in perceptual decision making. *The Journal of neuroscience : the official journal of the Society for Neuroscience* **32**, 6117-6125, doi:10.1523/JNEUROSCI.6489-11.2012 (2012).

43 Wiecki, T. V., Sofer, I. & Frank, M. J. HDDM: Hierarchical Bayesian estimation of the Drift-Diffusion Model in Python. *Frontiers in neuroinformatics* **7**, 14, doi:10.3389/fninf.2013.00014 (2013).

44 Ratcliff, R. & McKoon, G. The diffusion decision model: theory and data for two-choice decision tasks. *Neural Comput* **20**, 873--922, doi:10.1162/neco.2008.12-06-420 (2008).

45 Philiastides, M. G., Heekeren, H. R. & Sajda, P. Human Scalp Potentials Reflect a Mixture of Decision-Related Signals during Perceptual Choices. *Journal of Neuroscience* **34**, 16877--16889, doi:10.1523/JNEUROSCI.3012-14.2014 (2014).

46 Kiani, R., Corthell, L. & Shadlen, M. N. Choice certainty is informed by both evidence and decision time. *Neuron* **84**, 1329-1342, doi:10.1016/j.neuron.2014.12.015 (2014).

47 Siegel, M., Buschman, T. J. & Miller, E. K. Cortical information flowduring flexible sensorimotor decisions. *Science* **348**, 1352-1355, doi:10.1126/science.aab0551 (2015).

48 Gold, J. I. & Shadlen, M. N. The neural basis of decision making. *Annual review of neuroscience* **30**, 535-574, doi:10.1146/annurev.neuro.29.051605.113038 (2007).

49 Warbrick, T. *et al.* Single-trial P3 amplitude and latency informed event-related fMRI models yield different BOLD response patterns to a target detection task. *NeuroImage* **47**, 1532-1544, doi:10.1016/j.neuroimage.2009.05.082 (2009).

50 Walz, J. M. *et al.* Simultaneous EEG-fMRI reveals a temporal cascade of task-related and default-mode activations during a simple target detection task. *NeuroImage* **102 Pt 1**, 229-239, doi:10.1016/j.neuroimage.2013.08.014 (2014).

51 Yeung, N. & Summerfield, C. Metacognition in human decision-making: confidence and error monitoring. *Philosophical transactions of the Royal Society of London. Series B, Biological sciences* **367**, 1310-1321, doi:10.1098/rstb.2011.0416 (2012).

52 Steinhauser, M. & Yeung, N. Decision processes in human performance monitoring. *The Journal of neuroscience : the official journal of the Society for Neuroscience* **30**, 15643-15653, doi:10.1523/JNEUROSCI.1899-10.2010 (2010).

53 Gherman, S. & Philiastides, M. G. Neural representations of confidence emerge from the process of decision formation during perceptual choices. *NeuroImage* **106**, 134-143, doi:10.1016/j.neuroimage.2014.11.036 (2015).

786 54 Heereman, J., Walter, H. & Heekeren, H. R. A task-independent neural
787 representation of subjective certainty in visual perception. *Front Hum Neurosci* **9**,
788 551, doi:10.3389/fnhum.2015.00551 (2015).
789 55 Botvinick, M. M., Braver, T. S., Barch, D. M., Carter, C. S. & Cohen, J. D.
790 Conflict monitoring and cognitive control. *Psychological review* **108**, 624-652
791 (2001).
792 56 Dakin, S. C., Hess, R. F., Ledgeway, T. & Achtman, R. L. What causes non-
793 monotonic tuning of fMRI response to noisy images? *Current biology : CB* **12**,
794 R476-477; author reply R478 (2002).
795 57 Sajda, P., Goldman, R. I., Dyrholm, M. & Brown, T. R. *Signal Processing and*
796 *Machine Learning for Single-trial Analysis of Simultaneously Acquired EEG and*
797 *fMRI*. (Elsevier Inc., 2010).
798 58 Sajda, P., Goldman, R. I., Philiastides, M. G., Gerson, A. D. & Brown, T. R. A
799 System for Single-trial Analysis of Simultaneously Acquired EEG and fMRI.
800 *2007 3rd International IEEE/EMBS Conference on Neural Engineering*,
801 doi:10.1109/CNE.2007.369667 (2007).
802 59 Zhang, Y., Brady, M. & Smith, S. Segmentation of brain MR images through a
803 hidden Markov random field model and the expectation-maximization algorithm.
804 *IEEE transactions on medical imaging* **20**, 45--57, doi:10.1109/42.906424 (2001).
805 60 Greve, D. N. & Fischl, B. Accurate and robust brain image alignment using
806 boundary-based registration. *NeuroImage* **48**, 63--72,
807 doi:10.1016/j.neuroimage.2009.06.060 (2009).
808 61 Conroy, B. R., Walz, J. M. & Sajda, P. Fast bootstrapping and permutation testing
809 for assessing reproducibility and interpretability of multivariate FMRI decoding
810 models. *PloS one* **8**, e79271, doi:10.1371/journal.pone.0079271 (2013).
811 62 Sherwin, J. & Sajda, P. Musical experts recruit action-related neural structures in
812 harmonic anomaly detection: evidence for embodied cognition in expertise. *Brain*
813 *and Cognition* **83**, 190-202, doi:10.1016/j.bandc.2013.07.002 (2013).
814 63 Strang, G. Introduction to Linear Algebra. *Mathematics of Computation* **18**, 510,
815 doi:10.2307/2003783 (2003).
816 64 Nichols, T. & Hayasaka, S. Controlling the familywise error rate in functional
817 neuroimaging: a comparative review. *Statistical methods in medical research* **12**,
818 419--446, doi:10.1191/0962280203sm341ra (2003).
819 65 Mumford, J. A., Turner, B. O., Ashby, F. G. & Poldrack, R. A. Deconvolving
820 BOLD activation in event-related designs for multivoxel pattern classification
821 analyses. *NeuroImage* **59**, 2636-2643, doi:10.1016/j.neuroimage.2011.08.076
822 (2012).
823 66 Darlington, R. B. & Hayes, A. F. Combining independent p values: extensions of
824 the Stouffer and binomial methods. *Psychological methods* **5**, 496-515,
825 doi:10.1037/1082-989X.5.4.496 (2000).
826 67 Benjamini, Y. & Hochberg, Y. Controlling the False Discovery Rate: A Practical
827 and Powerful Approach to Multiple Testing. *Journal of the Royal Statistical*
828 *Society. Series B (Methodological)* **57**, 289 -- 300, doi:10.2307/2346101 (1995).
829 68 Smith, S. M. & Nichols, T. E. Threshold-free cluster enhancement: addressing
830 problems of smoothing, threshold dependence and localisation in cluster
831 inference. *NeuroImage* **44**, 83-98, doi:10.1016/j.neuroimage.2008.03.061 (2009).

69 Stephan, K. E. *et al.* Ten simple rules for dynamic causal modeling. *NeuroImage* **49**, 3099--3109, doi:10.1016/j.neuroimage.2009.11.015 (2010).

70 Penny, W. D. *et al.* Comparing families of dynamic causal models. *PLoS Computational Biology* **6**, doi:10.1371/journal.pcbi.1000709 (2010).

71 Bates, D., Mächler, M., Bolker, B. & Walker, S. Fitting Linear Mixed-Effects Models Using lme4. *2015* **67**, 48, doi:10.18637/jss.v067.i01 (2015).

## *Figure Captions*

Figure 1. **Paradigm and traditional EEG and fMRI results**

**A,** 3-AFC task where stimulus evidence for each category is modulated by varying the phase coherence in the images. **B,** Example of face images with high stimulus evidence (high coherence: 50%) and low stimulus evidence (low coherence: 35%). **C,** Behavioral performance shows significant differences, as a function of stimulus evidence, in accuracy ($p< 10^{-12}$, paired t-test) and **D,** response time ($p< 10^{-8}$, paired t-test) across the group. **E,** Grand average stimulus-locked event related potentials (ERPs) for electrode Pz show that differences in stimulus evidence span the time from stimulus to response. **F**, fMRI analysis showing cortical areas correlated with high (red) vs. low (blue) stimulus evidence across the entire trial ($Z> 2.57$ with $p< 0.01$ Family-Wise Error cluster corrected).

Figure 2. **Temporally precise trial-to-trial EEG variability tags brain regions during decision-making**

**A**, Illustration of how trial-to-trial variability of neural activity in spatially distinct cortical areas can be used to tag brain regions. In this hypothetical example Region 1 is involved in sensory encoding while Region 2 integrates sensory evidence to form a decision (in NHP literature, Region 1 might represent MT, while Region 2 LIP). Neural activity across the trial is shown for two stimulus types, one with high sensory evidence for the choice (red curves) and one with low sensory evidence (blue curves). Also shown are two temporal windows ($\tau_1$ and $\tau_2$) that represent different times during the trial. **B**, Linear classifiers are trained to separate trials based on the two levels of stimulus evidence at specific temporal windows. Shown are classifiers (parameterized by weight

vectors $w_1$ and $w_2$) for two temporal windows ($\tau_1$ and $\tau_2$) with respect to two EEG sensors (for simplicity only two dimensions of the full N=43 sensor space are shown. Though the component hyperplane is optimal for the full 43 dimensions, when projected to a line in two dimensions for illustration, it may appear that the separation is sub-optimal). This yields an EEG discriminant component for each temporal window. Variability along these components serves as a unique feature vector for temporally tagging the BOLD data—e.g. variability along an EEG component trained with data from $\tau_1$ tags BOLD voxels with time $\tau_1$ while variability along an EEG component trained with data from $\tau_2$ tags them with $\tau_2$.

Figure 3. **Encoding models based on stimulus derived features versus EEG variability**

**A**, A traditional encoding model used in fMRI analysis extracts a set of features from the stimulus that are potentially representative of low level structure and high level semantics (green box). Weights are learned to model how these stimulus features are encoded in the fMRI BOLD signal. The resulting encoding model is used to make predictions based on how well different voxels predict the features from novel stimuli. For example, one can create maps of the brain that are labeled based on the stimulus features that each voxel represents. **B**, The same encoding model concept applied to EEG variability (EEG encoding model). Instead of features being estimated from the stimulus, they are derived from EEG component trial-to-trial variability (as in Fig 2a) with each temporal window representing a different feature (green box). Weights are learned so as to model how the EEG variability at a given time window is encoded in the fMRI BOLD. As in the

887 traditional encoding model, predictions on novel stimuli can be done to test the model
888 and results can be used to construct a map —in this case a map of the brain that shows
889 the timing of the EEG component variability that each voxels represents.
890
891 Figure 4. **EEG discrimination and encoding model results**
892 **A,** Group average area under the receiver operating curve (AUC) for the sliding window
893 logistic regression EEG discrimination analysis, comparing high versus low stimulus
894 evidence trials; standard error across subjects is shown with shading. **B**, A single subject's
895 discriminating y-value distributions for high (red) and low stimulus evidence (blue) trials
896 for two EEG time points (225ms and 600ms). **C**, Significant fMRI voxels resulting from
897 the group level analysis for the encoding model ($p< 0.01$ TFCE-False Discovery Rate
898 (FDR) corrected). Activity is seen encompassing early visual processing regions,
899 attention networks, and the task positive network. **D**, A random subset of 100 (50 for
900 each stimulus evidence condition) from 700 total trials of the actual (circle) and predicted
901 (diamond) BOLD responses from the encoding model, for an example subject at a single
902 voxel (MNI X/Y/Zmm: -27/-54/-15, $r=0.206$, $p<10^{-6}$). High and low stimulus evidence
903 trials are shown separately for clarity. **E**, The averaged correlation of the predicted y-
904 values with the true y-values across the trial duration. Blue shading represents the
905 standard error across subjects. Grey shading indicates significant time windows ($p< 0.05$
906 FDR-corrected).
907
908 Figure 5. **Group-level encoding model weights results show neural activation cascade**

909 Subset of thresholded (p< 0.05 FDR-Corrected, k=10) group level statistical parametric
910 maps created by stTFCE randomization procedure on the encoding model weight
911 matrices show the progression of spatial activity across the trial. Activation can be seen
912 early in the trial in the occipital regions while progressing more anteriorly later in the trial
913 to executive control areas. Activations in red indicate areas where high stimulus evidence
914 trials had larger activations than low stimulus evidence trials, and blue the inverse.
915
916 Figure 6. **Spatial-temporal event-related activations show coordinated reactivations.**
917 **A,** Union across time windows of significant voxels for high (red) and low (blue)
918 stimulus evidence activations. Voxels with activations for both high and low conditions
919 (at different time windows) are displayed in green. Also shown are the encoding model
920 weights for specific voxels, including fusiform gyrus (FG-R):36/-51/-18, (FG-L):-42/-
921 42/-18, superior lateral occipital cortex (sLOC):24/-63/36, superior parietal lobule
922 (SPL):27/-51/54, anterior cingulate cortex (ACC):-6/24/30, intraparietal sulcus (IPS):-
923 30/-60/39, middle frontal gyrus (MFG):-45/27/30, middle temporal gyrus (MT):-57/-
924 60/0. Asterisks indicate significant windows. **B**, Sequence of significant weights showing
925 a "replay" of the network after the onset of ACC activation (shaded ellipse). "Replay" is
926 faster than the initial stimulus driven sequence and strongest for low evidence trials.
927
928 Figure 7. **Trial-to-trial reactivation correlates with decision confidence.**
929 Trial-to-trial reactivation amplitude ( $Y_{j,i}^{R}$ – see Methods) of "replay" correlates with
930 confidence proxy for both high (**A)** and low (**B**) stimulus evidence conditions. Error bars
931 represent standard errors across subjects. (**C**), Stimulus-locked replay activation clusters

and feature importance. **(inset)** Regions of interest used in computing the reactivation values for computing confidence proxy correlations. These regions were taken from significant group activations from 600-800ms post stimulus. Regions were then clustered (> 48 voxels) and a secondary analysis for feature importance was performed. Here, we removed each cluster before computing trial-to-trial reactivations and compared the slope of reactivation x confidence proxy when all clusters were present. Panel **C** shows the ranking of feature importance for each cluster (more negative % change = more importance). Negative changes in slopes show that by removing that cluster the slope of the correlation between reactivation and confidence decreases, indicating the importance of that cluster. Increases in slope indicate that the correlation is higher with that region removed.

943 **Figures:**

944

945

946

947

948

949

950

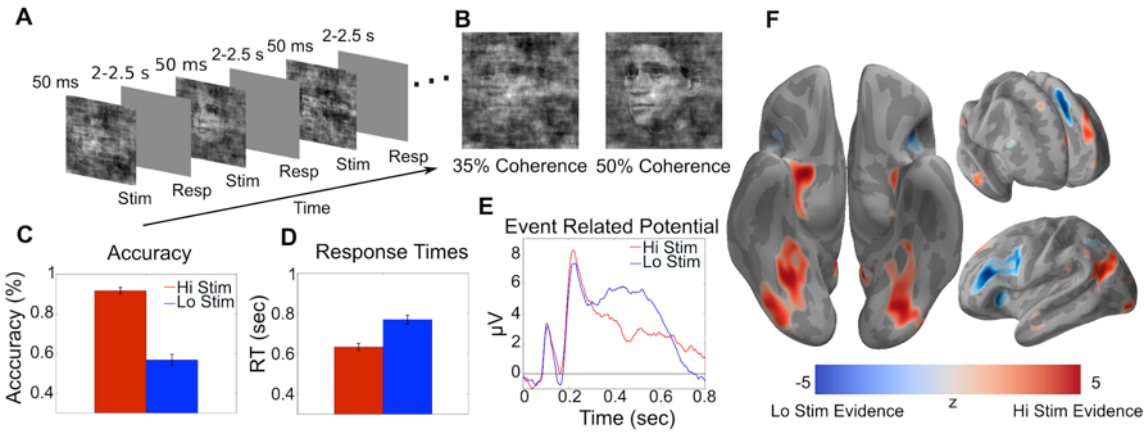


951

952 *Figure 1.*

953

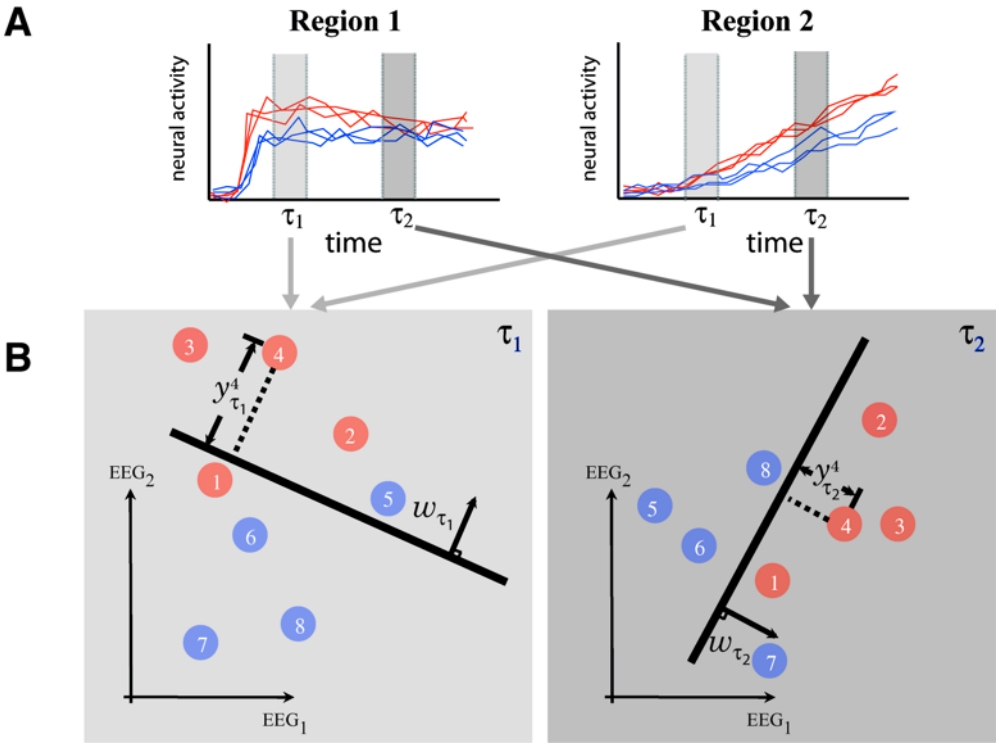


*Figure 2.*

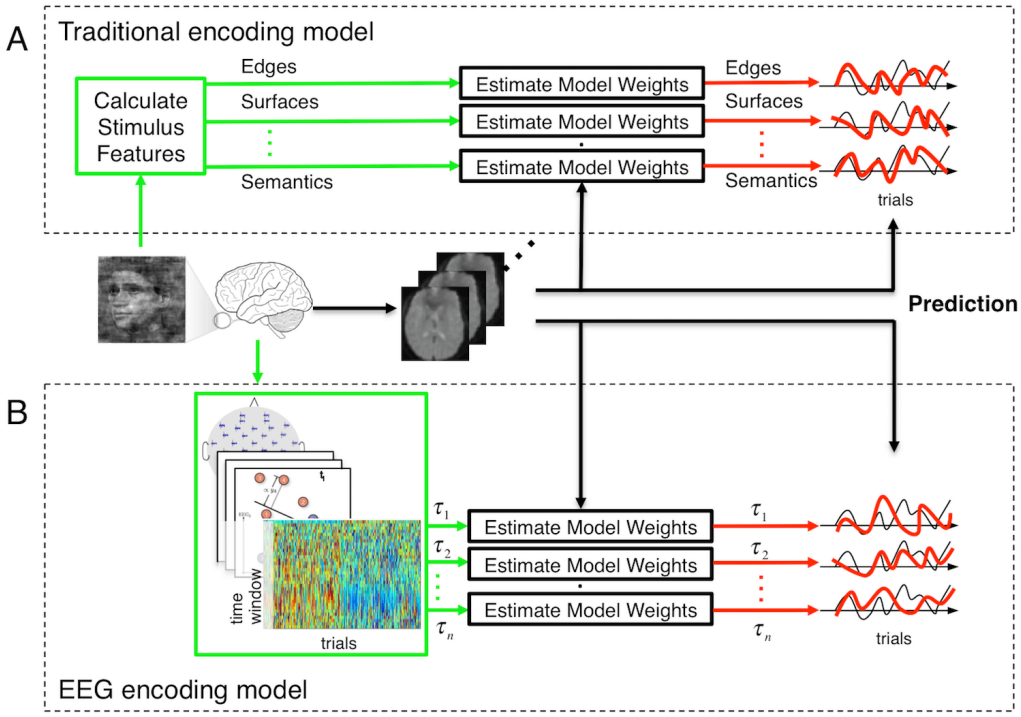


*Figure 3.*

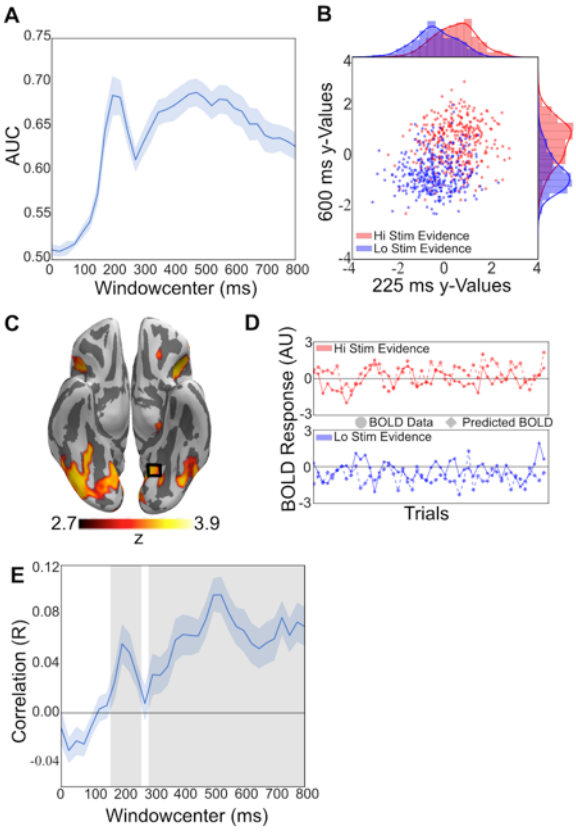


*Figure 4.*

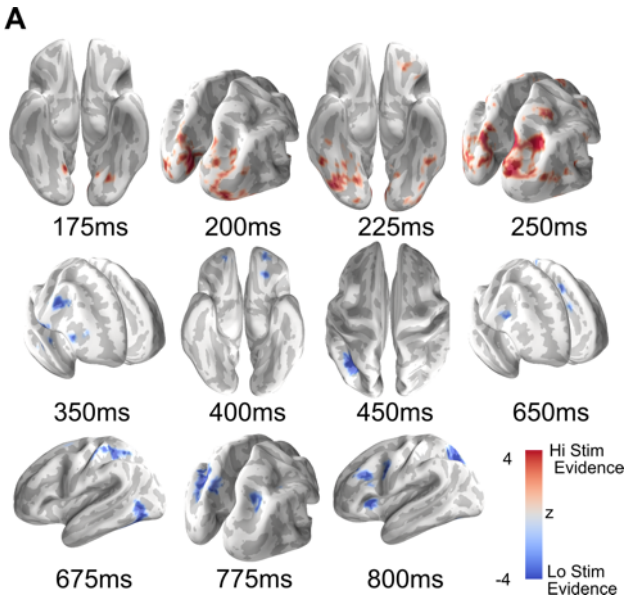


*Figure 5.*

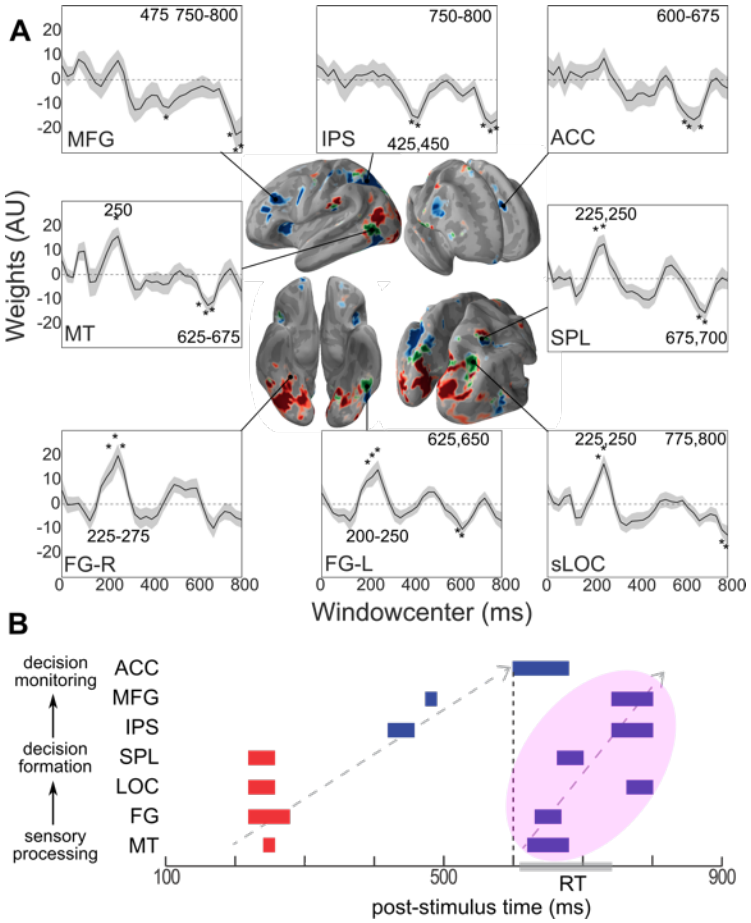


*Figure 6.*

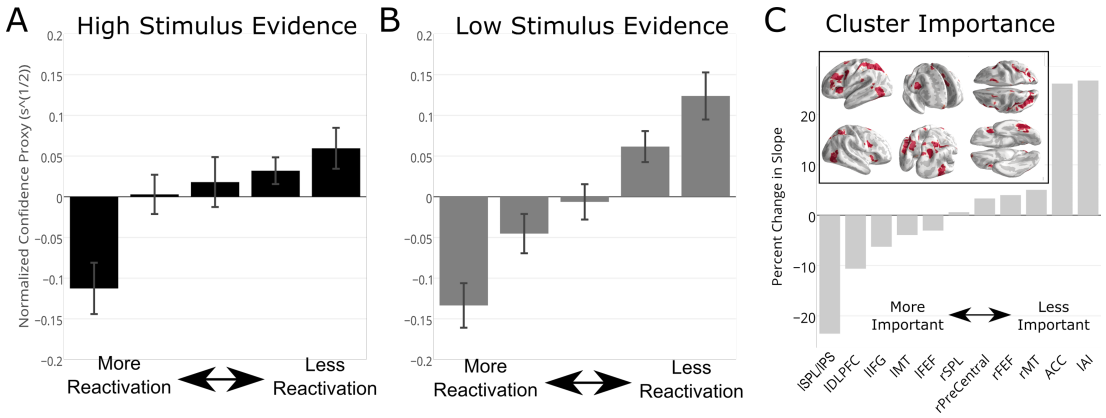


*Figure 7.*